

Faraday-rotation self-interference method for electron beam duration measurement in the laser wakefield accelerator

Jiaqi Liu (刘佳琦)^{1,2}, Wentao Li (李文涛)^{1,3,*}, Jiansheng Liu (刘建胜)^{1,4,**},
 Wentao Wang (王文涛)¹, Rong Qi (齐荣)¹, Zhijun Zhang (张志钧)¹,
 Changhai Yu (余昌海)¹, Zhiyong Qin (秦志勇)^{1,2}, Ming Fang (方明)^{1,2}, Ke Feng (冯珂)^{1,2},
 Ying Wu (吴颖)^{1,2}, Cheng Wang (王成)¹, and Ruxin Li (李儒新)^{1,4,5,***}

¹Shanghai Institute of Optics and Fine Mechanics, Chinese Academy of Sciences, Shanghai 201800, China

²University of Chinese Academy of Sciences, Beijing 100049, China

³Department of Physics, SUPA and University of Strathclyde, Glasgow G4 0NG, UK

⁴IFSA Collaborative Innovation Center, Shanghai Jiao Tong University, Shanghai 200240, China

⁵School of Physical Science and Technology, ShanghaiTech University, Shanghai 201210, China

*Corresponding author: wentao.li@strath.ac.uk; **corresponding author: michaeljs_liu@siom.ac.cn;

***corresponding author: ruxinli@mail.siom.ac.c

Received April 20, 2018; accepted May 21, 2018; posted online June 29, 2018

Real-time single-shot measurement of the femtosecond electron beam duration in laser wakefield accelerators is discussed for both experimental design and theoretical analysis that combines polarimetry and interferometry. The probe pulse polarization is rotated by the azimuthal magnetic field of the electron beam and then introduced into a Michelson-type interferometer for self-interference. The electron beam duration is obtained from the region size of the interference fringes, which is independent of the pulse width of the probe laser. Using a larger magnification system or incident angle, the measurement resolution can be less than 1 fs.

OCIS codes: 120.5410, 350.5400, 120.3180, 280.5395.

doi: 10.3788/COL201816.071202.

Great improvements have been achieved in laser wakefield accelerators (LWFAs) in the past few years^[1,2]. Stable quasi-monoenergetic electron beams from LWFAs are available using steady laser equipment and gas cells^[3,4]. Electron beams with GeV energy have also been demonstrated with self-injection^[4,5], ionization injection^[6,7] and cascaded LWFAs^[8]. This progress paved the road toward applications such as X-ray^[9] and γ -ray sources^[10]. The precise and complete diagnostics for the electron beams is necessary to extend these applications. Among all the parameters, some can be measured by traditional methods such as the energy spectrum and beam charge; others are completely beyond these methods' abilities. For instance, measurement of the electron beam duration is important for its application in the free-electron laser. Electro-optic techniques used in conventional accelerators can measure a beam duration of ~ 300 fs^[11]. However, according to the particle-in-cell (PIC) simulation^[12] and experimental^[8] results, the typical electron beam duration is shorter than 10 fs, which is too short to be measured by the traditional techniques.

Coherent transition radiation (CTR) in the THz spectral region, which is emitted when the electron beam transmits through a metal foil, has been used in a single-shot measurement of the electron beam duration longer than 30 fs^[13]. Near- to mid-infrared CTR spectroscopy has also been reported to be used to measure the electron beam duration within a few femtoseconds^[14], but it cannot work in the

single-shot mode and has a limited detecting range. Electron oscillation of its energy distribution caused by the laser field was also used to measure its duration^[15], but the electron beam quality would be affected during the measurement. Real-time measurement of beam duration by the magnetic field of the accelerated electron beam inside the wake has also been demonstrated^[16]. However, the length of the polarization-rotated probe laser τ_{rot} is the convolution of the beam duration τ_{beam} , transit time (time for the probe laser wave front transmitting through the azimuthal magnetic field region) τ_{trans} , imaging resolution τ_{res} , and probe laser duration τ_{pro} , which add quadratically. Among these parameters, τ_{pro} will sufficiently enlarge the result if it is longer than τ_{beam} . Additionally, τ_{pro} is sensitive to the group-velocity dispersion^[17], which also introduces inaccuracy in the beam duration. Therefore, a probe laser within 10 fs is required in this scheme. Such a short pulse is difficult to obtain with current facilities and additional synchronization equipment is required.

In this Letter, we discuss a Faraday-rotation self-interference (FRSI) method for femtosecond electron beam duration measurement from the aspects of experimental design and theoretical analysis. This method is a combination of the Faraday-rotation effect^[18] and a Michelson-type interferometer. The polarization of the probe laser is rotated by the azimuthal magnetic field of the electron beam, just as described in Ref. [16]. The difference is that the Glan-laser polarizer in the FRSI

method allows the transmission of the polarization-rotated light. Then the transmitted light is incident into a Michelson-type interferometer for self-interference. Because the region size of the interference fringes is only related to the magnetic field profile of the electron beam, the measurement result is independent of τ_{pro} . By adjusting the magnification and the angle between the interfering light beams, the electron beam duration resolution of the FRSI method can be shorter than 1 fs.

The FRSI method is based on two well-known techniques, the Faraday-rotation effect and the Michelson-type interferometer. The experimental setup for Faraday-rotation measurement is similar to the scheme in Ref. [16], as shown in Fig. 1. The probe light beam is split from the driving pulse, which propagates perpendicularly to the driver and accelerated electron beam. Because the electron beam in LWFA has a high energy, charge (~ 100 pC), and ultrashort duration (~ 10 fs), the generated current can be as high as ~ 10 kA, which leads to a co-moving strong azimuthal magnetic field. The azimuthal magnetic field is much higher than that generated by the displacement current in the bubble, which is homogenous in the longitudinal direction^[16]. The strong magnetic field of the electron beam will rotate the polarization of the probe laser passing above or below the electron beam inversely because of the Faraday-rotation effect. The angle of the probe laser polarization rotated by the azimuthal magnetic field \vec{B}_ϕ is calculated by

$$\varphi_{\text{rot}} = \frac{e}{2m_e c n_{\text{cr}}} \int_l n_e \vec{B}_\phi \cdot d\vec{s}, \quad (1)$$

where m_e , e , and c are the electron mass, electron charge, and speed of light in vacuum. $n_{\text{cr}} \approx 1.72 \times 10^{21} \text{ cm}^{-3}$ is the critical density for the pulse wavelength of $0.8 \mu\text{m}$, and n_e is the electron density. $d\vec{s}$ is the path element along the propagation path l of the probe pulse through the plasma region.

A Glan-laser polarizer with a 90° angle away from the initial probe pulse polarization is located before the

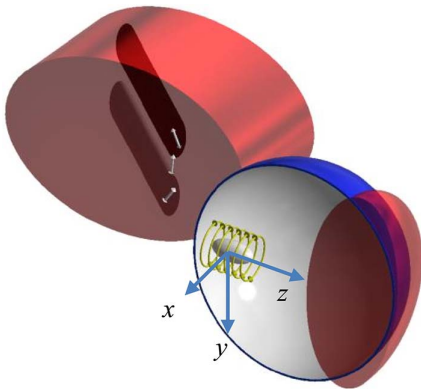


Fig. 1. Layout of the Faraday-rotation measurement. The polarizations of the light passing above and below the beam are rotated oppositely.

interferometer. The extinction ratio of the Glan-laser polarizer is $10^5:1$ so that it only allows the transmission of the polarization-rotated light by the magnetic field, as shown by two dark regions in a cylindrical shape in Fig. 1. Because the velocity of the electron beam is almost identical to the light speed, the dark cylindrical region is oblique. The angle between the axis of the cylinder and the propagation direction is 45° . Before the Michelson-type interferometer, the polarization-rotated region of the probe light is magnified N_1 times by a pair of lenses.

In the Michelson-type interferometer, the incident probe light is split into two beams (L1 and L2) by a 50:50 beam splitter. L1 is reflected and flipped horizontally by a mirror, as shown in Fig. 2. L2 is reflected and flipped by the right-angle prism and beam splitter. The cylindrical regions of L1 and L2 are symmetric around the z axis in the x - z plane. A small incident angle θ is introduced between the propagation directions of these two beams by adjusting the mirror. As a result, L1 and L2 interfere with each other in the overlapping region, which is recorded by a CCD camera after being amplified N_2 times by another amplification system. Since the region size of the interference fringes only depends on the scale of the magnetic field profile, which is not affected by the probe beam duration, the length of the electron beam can be determined from the region size of the interference fringes with high accuracy. The FRSI method does not require a short probe laser.

The distribution of the polarization rotation angle φ_{rot} on the probe pulse can be calculated from the PIC simulation result using Eq. (1). Figure 3(a) shows a typical magnetic field distribution of the electron beam in the transverse cross section in the self-injected LWFA simulation results with parameters of $a_0 = 2$ and $n_e = 6 \times 10^{18} \text{ cm}^{-3}$, where the electron beam

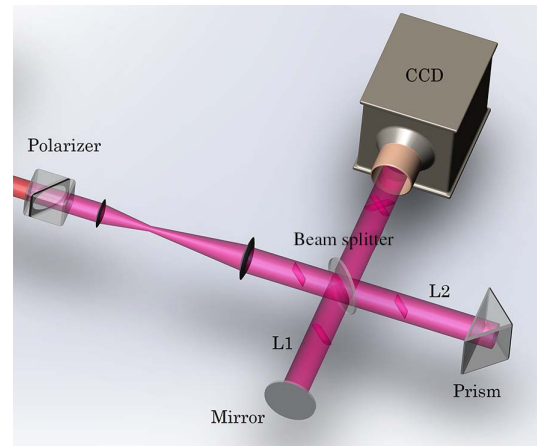


Fig. 2. Layout of the Michelson-type interferometer. The polarizer only allows the transmission of the polarization-rotated light. The probe beam is amplified N_1 times by a pair of lenses and then split into L1 and L2 by a beam splitter. L1 and L2 interfere with each other and the interference fringes are recorded by a CCD camera after being amplified N_2 times by another amplification system.

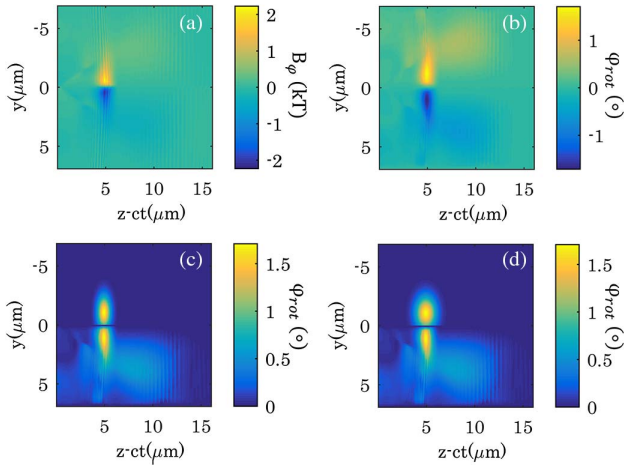


Fig. 3. (a) Magnetic field distribution of the electron beam and (b) the polarization rotation angle of the probe laser using Eq. (1) in the y - z plane from PIC simulations. The distribution of the polarization rotation angle of a Gaussian magnetic field profile (c) without and (d) with considering the transit time of the probe light.

propagates along the z axis. The average magnetic fields caused by the displacement current and accelerated electron beam are typically 0.2 and 1.7 kT, respectively. The polarization rotation angle can be calculated by tracking the magnetic field and electron density distribution in the propagation route of the probe light without considering the displacement of the electron beam during the transit time. Figure 3(b) shows the distribution of the polarization rotation angle φ_{rot} when the probe pulse propagates through the electron beam. The φ_{rot} caused by azimuthal magnetic field is larger than 1.2° , while the φ_{rot} introduced by the displacement current is usually $\sim 0.28^\circ$. However, because the magnetic field and φ_{rot} introduced by the displacement current are nearly homogeneous in the longitudinal direction, it has a negligible effect on the longitudinal extension of the polarization-rotated region. It is worth noting that the contributions to the region of the magnetic field from the electrons at the bubble vertex are not considered here, which would additionally overestimate the beam duration, especially for a low-energy electron beam.

To clarify the relation between the region size of the interference fringes and electron beam duration, the analytical description of the polarization rotation angle distribution is required in our scheme. Since the azimuthal magnetic field is rotationally symmetric around the z axis, and only the polarization of the light above and below the electron beam can be rotated by the magnetic field, φ_{rot} has inversion symmetry around the z axis. Therefore, we only consider the top half of the rotation angle for simplicity. The magnetic distribution can be further simplified by assuming that it has a Gaussian intensity profile in the y - z plane, where (0, 0) is defined as the position with the maximum polarization rotation angle φ_0 . The magnetic field region is assumed to have a full width at

half-maximum (FWHM) of r_{mag} along the y axis and a full length at half-maximum (FLHM) of L_{mag} along the z axis, where $L_{\text{mag}} = 0.92 \mu\text{m}$ and $r_{\text{mag}} = 1.28 \mu\text{m}$ are obtained from Fig. 3(b). Without considering the transit time of the probe laser, the distribution of the rotation angle φ_{rot} in the y - z plane is formulated as

$$\varphi_{\text{rot}}(y, z) = \varphi_0 \exp \left[-4 \ln 2 \left(\frac{y^2}{r_{\text{mag}}^2} + \frac{z^2}{L_{\text{mag}}^2} \right) \right]. \quad (2)$$

The polarization rotation angle distribution from Eq. (2) is shown in the top half of Fig. 3(c), which agrees well with the simulation result in the bottom half in Fig. 3(c). Further, if the transit time for the probe pulse wave front is approximated to be $2r_{\text{mag}}/c$, the polarization rotation angle is expressed as

$$\varphi_{\text{rot}}(y, z, t) = \varphi_0 \exp \left\{ -4 \ln 2 \left[\frac{y^2}{r_{\text{mag}}^2} + \frac{(z - ct)^2}{L_{\text{mag}}^2 + 4r_{\text{mag}}^2} \right] \right\}. \quad (3)$$

The profile is shown in the top half of Fig. 3(d), which is obviously wider along the z axis than the simulation result in the bottom half.

The probe laser pulse propagates along the x axis with the electric field described as $E(x, t) = E_0 \cos(\omega t - kx) \exp \left[-2 \ln 2 \left(\frac{x - ct}{\sigma_{\text{pro}}} \right)^2 \right]$. Its wavefront overlaps with the electron beam at $t = -\tau_{\text{pro}}$ and $x = 0$. When it is traveling through the magnetic field region, its polarization will be rotated by a small angle of $\varphi_{\text{rot}}(y, z, t)$. Using the Glan-laser polarizer, which is a 90° angle away from the initial probe pulse polarization, the transmitted electric field component is

$$E(x, y, z, t) = E_0 \varphi_0 \cos(\omega t - kx) \exp \left\{ -2 \ln 2 \left[\left(\frac{x - ct}{\sigma_{\text{pro}}} \right)^2 + \frac{2y^2}{r_{\text{mag}}^2} + \frac{2(z - ct)^2}{L_{\text{mag}}^2 + 4r_{\text{mag}}^2} \right] \right\}. \quad (4)$$

Since the polarization of the probe pulse can only be rotated when it passes through the magnetic field, the time range for Eq. (4) should be limited to from $-\tau_{\text{pro}}$ to τ_{pro} .

Before the probe light is incident into the interferometer, it is magnified N_1 times by a pair of lenses. Additionally, if the propagation distance of the electron beam within the probe light duration is considered, the axis of the transmitted region is 45° away from the initial propagation direction of the probe light. The electric field of the oblique cylinder in Fig. 1 can be expressed as

$$E(x, y, z, t) = E_0 \varphi_0 \cos(\omega t - kx) \exp \left\{ -2 \ln 2 \left[\left(\frac{x - ct}{\sigma_{\text{pro}}} \right)^2 + \frac{2y^2}{N_1^2 r_{\text{mag}}^2} + \frac{2(z + x - ct)^2}{N_1^2 (L_{\text{mag}}^2 + 4r_{\text{mag}}^2)} \right] \right\}. \quad (5)$$

The probe beam will be split equally into two beams, which are noted as L1 and L2 in Fig. 2. L1 is reflected

twice by the beam splitter and mirror, with the inclination angle staying 45° away from the x axis in the x - z plane. Meanwhile, L2 is reflected by the right-angle prism and beam splitter for three times, and its inclination angle becomes 135° away from the x axis. L1 and L2 are symmetrical around the z axis. They both propagate along the z axis before entering the CCD camera. The electric fields of L1 and L2 become

$$E_1(x, y, z, t) = \frac{1}{2} E_0 \varphi_0 \cos(\omega t - kz) \exp \left\{ -2 \ln 2 \left[\left(\frac{z - ct}{c\tau_{\text{pro}}} \right)^2 + \frac{2y^2}{N_1^2 r_{\text{mag}}^2} + \frac{2(z - x - ct)^2}{N_1^2 (L_{\text{mag}}^2 + 4r_{\text{mag}}^2)} \right] \right\}, \quad (6)$$

$$E_2(x, y, z, t) = \frac{1}{2} E_0 \varphi_0 \cos(\omega t - kz) \exp \left\{ -2 \ln 2 \left[\left(\frac{x - ct}{c\tau_{\text{pro}}} \right)^2 + \frac{2y^2}{N_1^2 r_{\text{mag}}^2} + \frac{2(z + x - ct)^2}{N_1^2 (L_{\text{mag}}^2 + 4r_{\text{mag}}^2)} \right] \right\}. \quad (7)$$

From Eqs. (6) and (7), the individual intensity profile of L1 or L2 integrated from $-\tau_{\text{pro}}$ to τ_{pro} will be affected by both the magnetic field region size and the probe pulse duration τ_{pro} . τ_{pro} will expand the size of the intensity profile along the x axis. By adjusting the position and angle of the right-angle prism, L1 and L2 can be normally incident to the CCD synchronously. However, if a tiny angle θ between the propagating direction of L1 and the z axis is introduced by adjusting the mirror, the electric field of L1 is modified as

$$E_1(x, y, z, t) \approx \frac{1}{2} E_0 \varphi_0 \cos[\omega t - k(z + x\theta)] \exp \left\{ -2 \ln 2 \left[\left(\frac{z - ct}{c\tau_{\text{pro}}} \right)^2 + \frac{2y^2}{N_1^2 r_{\text{mag}}^2} + \frac{2(z - x - ct)^2}{N_1^2 (L_{\text{mag}}^2 + 4r_{\text{mag}}^2)} \right] \right\}. \quad (8)$$

The intensity profile of the two probe beams in the overlapping region can be obtained by substituting Eqs. (7) and (8) into the equation

$$I(x, y, z, t) = |E_1(x, y, z, t) + E_2(x, y, z, t)|^2. \quad (9)$$

In the plane $z = z'$ in the overlapping region, the transverse intensity profile is

$$I_o(x, y) = \int_{-\tau_{\text{pro}}}^{\tau_{\text{pro}}} |E_1(x, y, z, t) + E_2(x, y, z, t)|^2 \delta(z - z') dt. \quad (10)$$

The interference term in Eq. (10) is

$$I_{12}(x, y) \propto I_{12} \int_{-\tau_{\text{pro}}}^{\tau_{\text{pro}}} \cos(kx\theta) \exp \left\{ -4 \ln 2 \left[\frac{(z' - ct)^2}{(c\tau_{\text{pro}})^2} + \frac{2y^2}{N_1^2 r_{\text{mag}}^2} + \frac{2x^2 + 2(z' - ct)^2}{N_1^2 (L_{\text{mag}}^2 + 4r_{\text{mag}}^2)} \right] \right\} dt. \quad (11)$$

From Eqs. (10) and (11), the intensity profile in the imaging plane x - y - z' of the overlapping region can be considered as the mixture of a background intensity profile and interference fringes. The scale of the background intensity profile will be expanded for both a larger magnetic field region and a longer τ_{pro} . However, as the term $\int_{-\tau_{\text{pro}}}^{\tau_{\text{pro}}} \exp \left\{ -4 \ln 2 \left[\frac{(z' - ct)^2}{(c\tau_{\text{pro}})^2} + \frac{2(z' - ct)^2}{N_1^2 (L_{\text{mag}}^2 + 4r_{\text{mag}}^2)} \right] \right\} dt$ only modulates the intensity envelope of the interference fringes, the region scale of the interference fringes in the x - y - z' plane is independent of τ_{pro} . The interference fringes are restricted in a range with FWHM sizes of $N_1 r_{\text{mag}} / \sqrt{2}$ along the y axis and $N_1 \sqrt{L_{\text{mag}}^2 + 4r_{\text{mag}}^2} / \sqrt{2}$ along the x axis. The fringe interval is only determined by θ . τ_{pro} only affects the intensity envelope of the interference fringes. Therefore, by measuring the height and the width of the interference region, the duration of the electron beam L_{mag} can be determined.

The magnetic field region radius and electron beam duration can be determined from the region size of the interference fringes. Here, we offer a theoretical example for explanation in which the probe beam has a duration of 100 fs, and the magnetic field has a length of 1.5 μm and radius of 2 μm . The beam waist of the polarization-rotated light is magnified 10 times after the polarizer by the magnification system; the angle θ between L1 and L2 is assumed to be 5° . The pixel size of the CCD camera is assumed to be 5 μm , considering a second

magnification system of $N_2 = 5$, and the resolution of CCD camera is improved to be 1 μm . Figure 4(a) shows the intensity distribution I_2 of the single beam L2 in the imaging plane x - y - z' , which is calculated from Eq. (7). Figure 4(b) shows the intensity profile I_o of L1 and L2 in the imaging plane from Eq. (10), which contains the interference fringes. Figures 4(c) and 4(d) present the normalized integral intensity traces along the y axis and x axis of the intensity profile in Fig. 4(a), respectively. Figure 4(e) shows the normalized integral intensity trace along the x axis of the intensity profile in Fig. 4(b). The interference fringes I_{12} are retrieved by $I_{12} = I_o - 2I_2$, and the normalized intensity trace along the x axis is plotted in Fig. 4(f). The scale of the interference fringes is

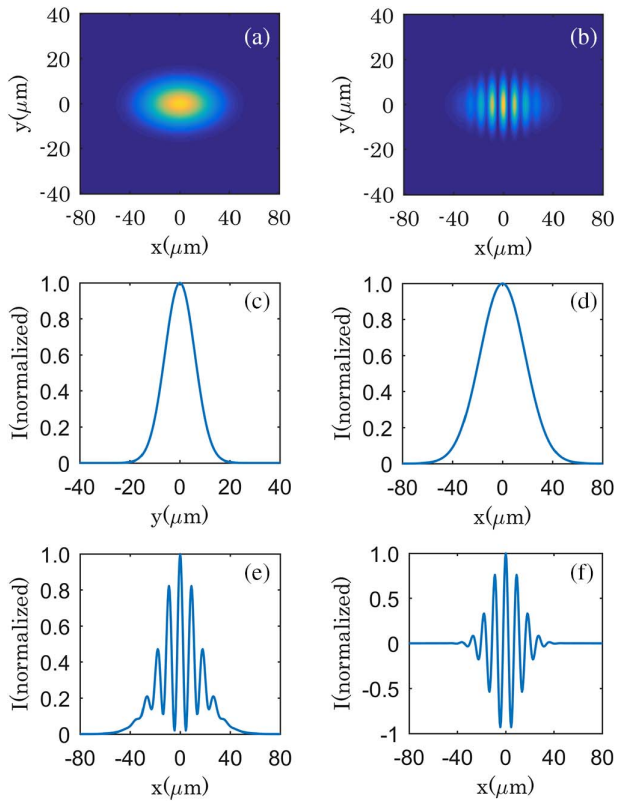


Fig. 4. Intensity distributions of (a) L2 from Eq. (7) and (b) L1 and L2 from Eq. (10) in the plane x - y - z' with $\tau_{\text{pro}} = 100$ fs; the normalized integral intensity traces of L2 along the (c) y axis and (d) x axis; (e) the normalized integral intensity profile of the overlapping region along the x axis; (f) the normalized intensity of the retrieved interference fringes in the x axis.

calculated from the intensity envelopes in Figs. 4(c) and 4(f), whose FWHM are $14 \mu\text{m}$ and $31 \mu\text{m}$, respectively. According to the analysis above, the radius r_{mag} and the duration L_{mag} of the magnetic field can be determined to be $1.98 \mu\text{m}$ and $1.88 \mu\text{m}$ (6.3 fs), which are quite consistent with the preset values.

With the FRSI method, the electron beam can even be measured by the probe beam with a longer pulse duration because the region size of the interference fringes is not influenced by τ_{pro} . This is more obvious if the duration of the probe laser is increased from 100 fs to 250 fs, with other parameters unchanged. For measurement without self-interference, the intensity profile in the imaging plane will be widened in the x direction due to the contribution of the probe beam duration, as shown in Figs. 5(a) and 5(d). Meanwhile, the width of the background intensity profile along the y axis in Fig. 5(c) is unchanged compared to the result in Fig. 4(c). The intensity profile in the imaging plane also has a larger scale along the x axis, as presented in Figs. 5(b) and 5(e), compared with those in Figs. 4(b) and 4(e). However, the retrieved intensity profile of the interference fringes in Fig. 5(f) is the same as the result in Fig. 4(f), which means that the measurement results are the same for a longer τ_{pro} . Additionally, as the FRSI method does not require the stability or quality

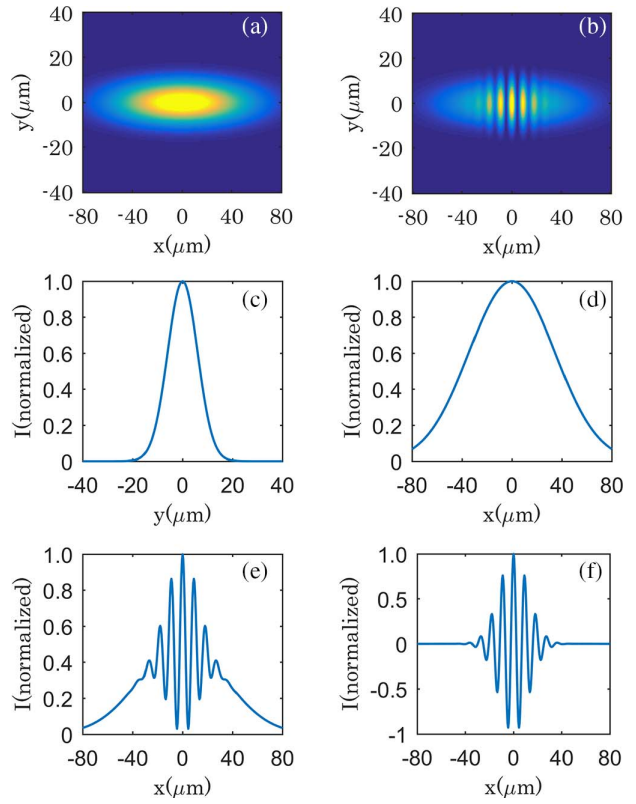


Fig. 5. Intensity distributions of (a) L2 from Eq. (7) and (b) L1 and L2 from Eq. (10) in the plane x - y - z' with $\tau_{\text{pro}} = 250$ fs; the normalized integral intensity traces of L2 along the (c) y axis and (d) x axis; (e) the normalized integral intensity profile of the overlapping region along the x axis; (f) the normalized intensity of the interference fringes in the x axis.

of the electron beam, it can realize the real-time and single-shot measurement.

In the FRSI method, the most important process is identifying the interference fringes from the background intensity profile. Since the region size of the magnetic field is characterized by the interference fringes, the measuring error is determined by the fringe interval η . If η is too large, measurement of the region size is inaccurate. As η is inversely proportional to the angle θ between L1 and L2 as $\eta = \lambda/\theta$, the inaccuracy is smaller at a larger θ , as shown in Fig. 6(a). However, η has to be larger than the pixel size Δs of the CCD camera in case the fringes are too close to identify, which limits the range of θ . The resolution of the second magnification system before the CCD camera, which is $\eta \approx \lambda/(2\theta N_2)$, also affects the determination of the region size. The corresponding error in determination of the electron beam duration is $\Delta\tau = \eta/c$. In the case in Figs. 4 and 5, the duration resolution is ~ 3 fs. As plotted in Fig. 6(b), $\Delta\tau$ declines with the improvement of N_2 and θ . For instance, the measurement error will be as small as ~ 0.76 fs if $N_2 = 20$ and $\theta = 5^\circ$. Moreover, the measurement inaccuracy of the electron beam duration is limited by the CCD pixel size as $\Delta L_{\text{mag}} = \pm \Delta s \sqrt{L_{\text{mag}}^2 + 4r_{\text{mag}}^2} / (\sqrt{2}N_1N_2L_{\text{mag}})$. In the cases in Figs. 4 and 5, ΔL_{mag} is nearly $\pm 0.17 \mu\text{m}$ (0.6 fs).

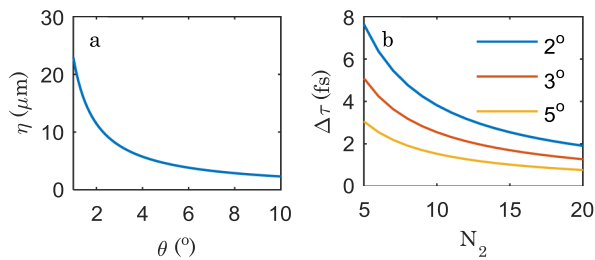


Fig. 6. (a) Interference fringe interval vs. the incident angle between L1 and L2. (b) The resolution of the measurement as a function of N_2 for different angles.

In this Letter, we design and analyze the FRSI method for the electron beam duration measurement in LWFAs, which is based on the Faraday-rotation effect and a Michelson-type interferometer. The polarization-rotated light by the azimuthal magnetic field of the electron beam is introduced into the interferometer to interfere with itself. Because the region size of the interference fringes is only related to the electron beam length and the radius of the magnetic region, the electron beam length measurement is independent of the pulse duration of the probe laser. The measurement error of the beam duration could be reduced to less than 1 fs with a higher magnification and larger incident angle.

This work was supported by the National Natural Science Foundation of China (Nos. 11127901, 11425418, 11505263, and 61521093), the Strategic Priority Research Program (B) (No. XDB16), Shanghai Sailing Program (Nos. 17YF1421100 and 18YF1426000), the Youth Innovation Promotion Association CAS, and the State Key Laboratory Program of the Chinese Ministry of Science and Technology.

References

1. F. S. Tsung, R. Narang, W. B. Mori, C. Joshi, R. A. Fonseca, and L. O. Silva, *Phys. Rev. Lett.* **93**, 185002 (2004).
2. W. P. Leemans, B. Nagler, A. J. Gonsalves, C. Toth, K. Nakamura, C. G. R. Geddes, E. Esarey, C. B. Schroeder, and S. M. Hooker, *Nat. Phys.* **2**, 696 (2006).
3. S. P. D. Mangles, C. D. Murphy, Z. Najmudin, A. G. R. Thomas, J. L. Collier, A. E. Dangor, E. J. Divall, P. S. Foster, J. G. Gallacher, C. J. Hooker, D. A. Jaroszynski, A. J. Langley, W. B. Mori, P. A. Norreys, F. S. Tsung, R. Viskup, B. R. Walton, and K. Krushelnick, *Nature* **431**, 535 (2004).
4. X. Wang, R. Zgadzaj, N. Fazel, Z. Li, S. A. Yi, X. Zhang, W. Henderson, Y. Y. Chang, R. Korzekwa, H. E. Tsai, C. H. Pai, H. Quevedo, G. Dyer, E. Gaul, M. Martinez, A. C. Bernstein, T. Borger, M. Spinks, M. Donovan, V. Khudik, G. Shvets, T. Ditmire, and M. C. Downer, *Nat. Commun.* **4**, 1988 (2013).
5. W. P. Leemans, A. J. Gonsalves, H. S. Mao, K. Nakamura, C. Benedetti, C. B. Schroeder, C. Toth, J. Daniels, D. E. Mittelberger, S. S. Bulanov, J. L. Vay, C. G. R. Geddes, and E. Esarey, *Phys. Rev. Lett.* **113**, 245002 (2014).
6. X. L. Xu, C. H. Pai, C. J. Zhang, F. Li, Y. Wan, Y. P. Wu, J. F. Hua, W. Lu, W. An, P. Yu, C. Joshi, and W. B. Mori, *Phys. Rev. Lett.* **117**, 034801 (2016).
7. M. Mirzaie, S. Li, M. Zeng, N. A. M. Hafz, M. Chen, G. Y. Li, Q. J. Zhu, H. Liao, T. Sokollik, F. Liu, Y. Y. Ma, L. M. Chen, Z. M. Sheng, and J. Zhang, *Sci. Rep.* **5**, 14659 (2015).
8. W. T. Wang, W. T. Li, J. S. Liu, Z. J. Zhang, R. Qi, C. H. Yu, J. Q. Liu, M. Fang, Z. Y. Qin, C. Wang, Y. Xu, F. X. Wu, Y. X. Leng, R. X. Li, and Z. Z. Xu, *Phys. Rev. Lett.* **117**, 124801 (2016).
9. K. Nakajima, *Proc. Japn. Acad. Ser. B* **91**, 223 (2015).
10. K. Ta Phuoc, S. Corde, C. Thauray, V. Malka, A. Tafzi, J. P. Goddet, R. C. Shah, S. Sebban, and A. Rousse, *Nat. Photonics* **6**, 308 (2012).
11. G. Berden, S. P. Jamison, A. M. MacLeod, W. A. Gillespie, B. Redlich, and A. F. G. van der Meer, *Phys. Rev. Lett.* **93**, 114802 (2004).
12. M. Geissler, J. Schreiber, and J. Meyer-ter-Vehn, *New J. Phys.* **8**, 186 (2006).
13. A. D. Debus, M. Bussmann, U. Schramm, R. Sauerbrey, C. D. Murphy, Z. Major, R. Hoerlein, L. Veisz, K. Schmid, J. Schreiber, K. Witte, S. P. Jamison, J. G. Gallacher, D. A. Jaroszynski, M. C. Kaluza, B. Hidding, S. Kiselev, R. Heathcote, P. S. Foster, D. Neely, E. J. Divall, C. J. Hooker, J. M. Smith, K. Ertel, A. J. Langley, P. Norreys, J. L. Collier, and S. Karsch, *Phys. Rev. Lett.* **104**, 084802 (2010).
14. O. Lundh, J. Lim, C. Rechatin, L. Ammoura, A. Ben-Ismael, X. Davoine, G. Gallot, J. P. Goddet, E. Lefebvre, V. Malka, and J. Faure, *Nat. Phys.* **7**, 219 (2011).
15. H. Kotaki, K. Kawase, Y. Hayashi, M. Mori, M. Kando, J. K. Koga, and S. V. Bulanov, *J. Phys. Soc. Jpn.* **84**, 074501 (2015).
16. A. Buck, M. Nicolai, K. Schmid, C. M. S. Sears, A. Saevart, J. M. Mikhailova, F. Krausz, M. C. Kaluza, and L. Veisz, *Nat. Phys.* **7**, 543 (2011).
17. M. S. Bigelow, N. N. Lepeshkin, H. Shin, and R. W. Boyd, *J. Phys. Condens. Mat.* **18**, 3117 (2006).
18. J. A. Stamper and B. H. Ripin, *Phys. Rev. Lett.* **34**, 138 (1975).